PHYSICAL REVIEW D **94,** 063527 (2016)

Dark matter astrophysical uncertainties and the neutrino floor

Ciaran A. J. O'Hare*

School of Physics and Astronomy, University of Nottingham, University Park, Nottingham NG7 2RD, United Kingdom

(Received 14 April 2016; revised manuscript received 15 August 2016; published 26 September 2016)

The search for weakly interacting massive particles (WIMPs) by direct detection faces an encroaching background due to coherent neutrino-nucleus scattering. For a given WIMP mass the cross section at which neutrinos constitute a dominant background is dependent on the uncertainty on the flux of each neutrino source, principally from the Sun, supernovae or atmospheric cosmic ray collisions. However there are also considerable uncertainties with regard to the astrophysical ingredients of the predicted WIMP signal. Uncertainties in the velocity of the Sun with respect to the Milky Way dark matter halo, the local density of WIMPs, and the shape of the local WIMP speed distribution all have an effect on the expected event rate in direct detection experiments and hence will change the region of the WIMP parameter space for which neutrinos are a significant background. In this work we extend the neutrino floor calculation to account for the uncertainty in the astrophysics dependence of the WIMP signal. We show the effect of uncertainties on projected discovery limits with an emphasis on low WIMP masses (less than 10 GeV) when solar neutrino backgrounds are most important. We find that accounting for astrophysical uncertainties changes the shape of the neutrino floor as a function of WIMP mass but also causes it to appear at cross sections up to an order of magnitude larger, extremely close to existing experimental limits, indicating that neutrino backgrounds will become an issue sooner than previously thought. We also explore how neutrinos hinder the estimation of WIMP parameters and how astrophysical uncertainties impact the discrimination of WIMPs and neutrinos with the use of their respective time dependencies.

DOI: 10.1103/PhysRevD.94.063527

I. INTRODUCTION

The nature and detection of dark matter is one of the most pressing unsolved problems in modern physics. A myriad of cosmological observations indicate that ∼30% of the energy density of the Universe must be comprised of a cold and nonbaryonic component, yet the particle content of this dark matter remains unknown [1]. The most promising method of detecting dark matter in the laboratory is the search for their keV-scale nuclear recoils produced in elastic scattering events between dark matter particles in the Milky Way halo and target nuclei [2]. This method of detection is possible if dark matter is in the form of a weakly interacting massive particle (WIMP). These particles are a popular and well-motivated candidate which appear in extensions to the Standard Model such as supersymmetry, and freeze out in the early Universe with an abundance that matches cosmological observations (for reviews see, e.g., Refs. [3,4]).

Neutrinos are also weakly interacting particles. It is known that they must, too, elastically scatter off the same target nuclei of dark matter detectors. As a result of neutrinos being impossible to shield against, they are regarded as the ultimate background to experimental searches for WIMPs [5]. Current experiments such as Xenon100 [6], LUX [7], and CDMS [8], which can probe to spin-independent (SI) WIMP-nucleon cross sections of the order $\sigma_{\chi-n} \approx 10^{-44}$–$10^{-45}$ cm^2, are not yet sensitive to the expected neutrino background (for a recent review of direct detection experiments see, e.g., Ref. [9]). However as the sensitivity of experiments increases with the next generation of ton-scale (and beyond) detectors such as Xenon1T [10] and LZ [11], the neutrino background will begin to become important [5,12–14]. The boundary in the WIMP mass–cross section parameter space below which neutrinos are a problematic background is known as the neutrino floor and is caused by a close similarity between the recoil energies and rates of WIMPs of certain masses and cross sections [5,13–15]. For example in a Xenon detector the recoil energy spectrum of a WIMP with mass $m_\chi = 6$ GeV and SI cross section $\sigma_{\chi-n} \sim 5 \times 10^{-45}$ cm^2 very closely matches that of ^{8}B solar neutrinos [13].

The neutrino floor is not however the true final limit to direct detection. As initially shown by Ruppin *et al.* [16], the differences in the tails of the recoil energy distributions of WIMPs and neutrinos allow the "floor" to be overcome with high statistics [typically $> \mathcal{O}(1000)$ events]. Furthermore other studies have shown that the neutrino background can be mitigated with the use of annual modulation effects [17], direction dependence [18–20] or complementarity between multiple target nuclei [16]. A recent work by Dent *et al.* [21] made use of the nonrelativistic effective field theory formalism which posits additional operators to describe the nuclear response to a

*ciaran.ohare@nottingham.ac.uk

WIMP interaction. They found that for many of these additional operators, which induce significantly different nuclear recoil energy spectra, the neutrino bound is much weaker or not present. However the limits calculated by these studies all depend on the choice of astrophysical input; hence if an accurate prediction is to be made about when future experiments will be affected by the neutrino background at a statistically significant level, we must first establish the extent to which the uncertainty in the astrophysical input plays a role.

The phase space structure of the Milky Way halo in the region of the Solar System is an uncertain and much debated topic [22–24]. Most direct detection analyses use an isotropic and isothermal spherically symmetric assumption for the Galactic halo known as the standard halo model (SHM). This model gives rise to an isotropic Maxwellian velocity distribution for which there is an analytic form for the WIMP event rate. However substantial evidence from N-body and hydrodynamic simulations indicates that the velocity structure is likely to contain significant deviations from this simple Maxwellian form [25–27]. In extreme cases there is some evidence that the velocity distribution may contain highly anisotropic features such as tidal streams [28,29], a dark disk [30–33] and debris flows [34,35] which have been shown to have a noticeable effect on direct detection signals [36–38]. To add further complication, the astrophysical parameters not related to the velocity distribution directly such as the laboratory velocity $\mathbf{v}_{\rm lab}$ and local density ρ_0 are also subject to a high degree of uncertainty [39]. Particularly in the case of the local density this is a source of concern as it is degenerate with the WIMP-nucleon cross section. Attempts have been made however to account for astrophysical uncertainties in direct detection analyses by calculating halo-independent discovery limits [40–43]. In this work we include these astrophysical uncertainties in the neutrino floor calculation introduced in Ref. [15].

The outline of this paper is as follows. In Sec. II we present the nuclear recoil event rates in the case of WIMP and neutrino elastic scattering. Then in Sec. III we outline the profile likelihood test used to calculate the neutrino floor. In Sec. IV we describe the various sources of astrophysical uncertainty and how estimates on each parameter and the assumption of various different speed distributions alter the neutrino floor individually. In Sec. V we discuss the impact of astrophysical uncertainties on the potential for the upcoming generation of direct detection experiments to detect coherent neutrino-nucleus scattering, and Sec. VI deals with the effect of the same uncertainties on the parameter constraints possible in the event that a WIMP signal is detected. Then in Sec. VII we show how it is possible to probe beyond the neutrino floor by including the time dependence of the WIMP and solar neutrino event rates even once astrophysical uncertainties have been considered. Finally in Sec. VIII we summarize our results and conclude.

II. EVENT RATES

A. WIMPs

The elastic scattering event rate as a function of recoil energy and time assuming spin-independent interactions with identical couplings to protons and neutrons is given by [44]

$$\frac{\mathrm{d}R_\chi}{\mathrm{d}E_r} = \frac{\rho_0 \sigma_{\chi-n}}{2 m_\chi \mu_{\chi n}^2} A^2 F^2(E_r) g(v_{\rm min}, t), \tag{1}$$

where m_χ is the WIMP mass, $\mu_{\chi n}$ is the WIMP-nucleon reduced mass, ρ_0 is the local dark matter density, A is the mass number of the target and $\sigma_{\chi-n}$ is the WIMP-nucleon cross section. The function $F(E_r)$ is the form factor of the nucleus which only has a noticeable effect at large WIMP masses. In this work we will primarily be concerned with light WIMPs where understanding the neutrino background is most important; hence we will assume the standard Helm form factor for simplicity. Finally, $g(v_{\rm min}, t)$ is the mean inverse speed which is calculated by integrating the velocity distribution $f(\mathbf{v})$ from $v_{\rm min} = \sqrt{2 m_N E}/2\mu_{\chi n}$, the minimum WIMP speed required to produce a nuclear recoil of energy E_r,

$$g(v_{\rm min}, t) = \int_{v_{\rm min}}^{\infty} \frac{f(\mathbf{v} + \mathbf{v}_{\rm lab}(t))}{v} \mathrm{d}^3 v. \tag{2}$$

The lab velocity, $\mathbf{v}_{\rm lab}$, is the velocity of the observer relative to the rest frame of the Galaxy and if taken to be time dependent is responsible for the annual modulation of the event rate [45].

B. Neutrinos

For the keV-scale nuclear recoils relevant for WIMP detection the most important neutrino interaction to consider is coherent neutrino-nucleus scattering (CNS). We will ignore neutrino-electron elastic scattering, which for direct detection experiments has a very small event rate (from pp neutrinos) and only slightly adjusts the neutrino floor for WIMP masses larger than $\sim$100 GeV [15]. Despite the fact that CNS is yet to be observed, the rate is fully predicted by the Standard Model [46]. The differential cross section as a function of nuclear recoil energy (E_r) and neutrino energy (E_ν) is

$$\frac{\mathrm{d}\sigma}{\mathrm{d}E_r}(E_r, E_\nu) = \frac{G_F^2}{4\pi} Q_W^2 m_N \left(1 - \frac{m_N E_r}{2E_\nu^2}\right) F^2(E_r), \tag{3}$$

where $Q_W = \mathcal{N} - (1 - 4\sin^2\theta_W)\mathcal{Z}$ is the weak nuclear hypercharge of a nucleus with $\mathcal{N}$ neutrons and $\mathcal{Z}$ protons, G_F is the Fermi coupling constant, θ_W is the weak mixing angle and m_N is the nucleus mass. The event rate per unit mass, as a function of the recoil energy, is found by integrating the differential cross section with the neutrino

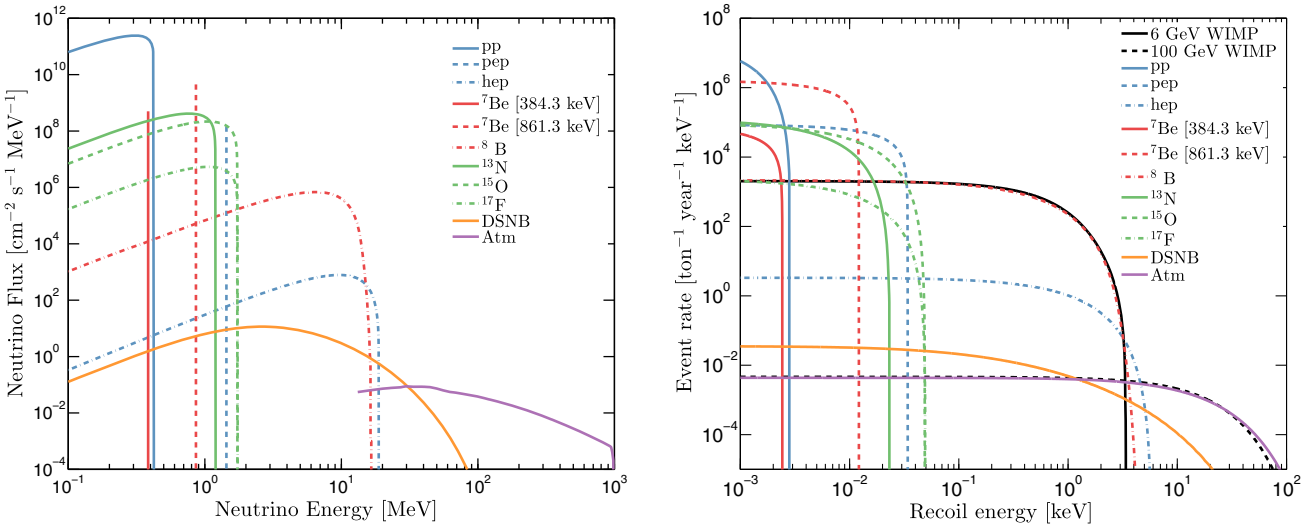

FIG. 1. Left: Neutrino energy spectra that are backgrounds to direct detection experiments: solar, atmospheric, and the diffuse supernova background. The atmospheric neutrino spectrum is the sum of contributions from electrons, antielectrons, muons and antimuons. The diffuse supernova background is the sum of three different neutrino temperatures, 3, 5 and 8 MeV. Right: Xenon scattering event rate as a function of recoil energy for each type of neutrino as well as a 6 GeV WIMP with $\sigma_{\chi-n} = 5 \times 10^{-45}$ cm^2 (solid black line) and a 100 GeV WIMP with $\sigma_{\chi-n} = 2.5 \times 10^{-49}$ cm^2 (dashed black line).

flux from $E_\nu^{\min} = \sqrt{m_N E_r/2}$, which is the minimum neutrino energy required to generate a nuclear recoil with energy E_r,

$$\frac{\mathrm{d}R_\nu}{\mathrm{d}E_r} = \int_{E_\nu^{\min}} \frac{\mathrm{d}\sigma}{\mathrm{d}E_r}\frac{\mathrm{d}\Phi}{\mathrm{d}E_\nu}\mathrm{d}E_\nu. \tag{4}$$

The neutrino flux Φ is the sum of multiple different components each with different individual energies and uncertainties. The relevant contributions to the neutrino background for WIMP searches are displayed in the left panel of Fig. 1 with uncertainties listed in Table I. In fact with advances in technology currently under way [47] it will be possible for direct detection experiments to make competitive measurements of these neutrino fluxes [48] and even constrain new physics such as the existence of sterile neutrinos [49] or new interactions between neutrinos and nuclei or electrons [50].

TABLE I. Total neutrino fluxes with corresponding uncertainties. All solar neutrino fluxes are from the updated high-metallicity SSM (Ref. [51]) with the exception of ^{8}B which is from an analysis of neutrino data (Ref. [52]). The DSNB and atmospheric neutrino fluxes are from Refs. [53] and [54] respectively. The maximum neutrino energy, $E_\nu^{\max}$, and maximum recoil energy of a Xenon target, $E_{r_{\mathrm{Xe}}}^{\max}$, are also shown.

ν type	$E_\nu^{\max}$ (MeV)	$E_{r_{\mathrm{Xe}}}^{\max}$ (keV)	ν flux (cm^{-2} s^{-1})
pp	0.42341	2.94×10^{-3}	$(5.98 \pm 0.036) \times 10^{10}$
^{7}Be	0.8613	0.0122	$(5.00 \pm 0.35) \times 10^{9}$
pep	1.440	0.0340	$(1.44 \pm 0.017) \times 10^{8}$
^{13}N	1.199	0.02356	$(2.96 \pm 0.41) \times 10^{8}$
^{15}O	1.732	0.04917	$(2.23 \pm 0.34) \times 10^{8}$
^{17}F	1.740	0.04962	$(5.52 \pm 0.94) \times 10^{6}$
^{8}B	16.360	4.494	$(5.16 \pm 0.11) \times 10^{6}$
hep	18.784	5.7817	$(8.04 \pm 2.41) \times 10^{3}$
DSNB	91.201	136.1	85.5 ± 42.7
Atm.	981.748	15.55×10^{3}	10.5 ± 2.1

Neutrinos from various fusion reactions in the interior of the Sun dominate the low-energy, high-flux regime and are the major neutrino background for direct detection with a total flux at Earth of around 6.5×10^{11} cm^{-2} s^{-1} [55,56]. Neutrinos from the initial pp reaction make up 86% of all solar neutrinos and have been detected most recently by the Borexino experiment, determining the flux with an uncertainty of ~10% [57]. For all neutrino fluxes other than ^{8}B the theoretical uncertainty is smaller than the measurement uncertainty. In this work we base our neutrino flux values and uncertainties on the high-metallicity standard solar model (SSM) calculation of Grevesse and Sauval [58], using values presented in Ref. [51] which are based on updated fusion cross sections [59]. However for the ^{8}B neutrino flux, a better estimate is found from considering current measurements; in this case we use the result presented in Ref. [52] based on a global analysis of all solar and terrestrial neutrino data.

For WIMP masses between 10 and 30 GeV, the neutrino floor is caused by the subdominant diffuse supernova neutrino background (DSNB), the sum total of all neutrinos emitted from supernovae over the history of the Universe. The background flux is calculated by performing a line of sight integral of the spectrum of neutrinos from a single supernova with the rate density of core-collapse supernovae as a function of redshift. See Ref. [53] for the

full calculation of the predicted DSNB. The total flux of the DSNB ($\sim 86\ \mathrm{cm}^{-2}\,\mathrm{s}^{-1}$) is considerably smaller than for solar neutrinos; however they are an important background to consider as supernovae neutrinos extend to a higher energy range not occupied by solar neutrinos. The calculated spectra have a Fermi-Dirac form with temperatures in the range 3 to 8 MeV. In this study we use a DSNB flux which is the sum of three temperatures: 3 and 5 MeV for electron and antielectron neutrinos respectively, and 8 MeV for the sum of the remaining neutrino flavors. There are considerable theoretical uncertainties in this calculation; hence we will take a large systematic uncertainty of 50% on the total flux of DSNB neutrinos [53].

The final type of neutrino remaining to be discussed is that from the atmosphere which provides the main neutrino background for WIMP masses above 100 GeV. These neutrinos occupy the high-energy and low-flux regime and will limit the sensitivity of experiments to spin-independent cross sections below around $10^{-48}\ \mathrm{cm}^2$ [13,15,16]. The flux of atmospheric neutrinos with energies less than 100 MeV is difficult to measure as well as predict theoretically [54,60,61] although the expected flux is around $11\ \mathrm{cm}^{-2}\,\mathrm{s}^{-1}$. In this work we use a calculation that is a sum of the contributions from electron, antielectron, muon and antimuon neutrinos and place a $\sim 20\%$ uncertainty on the total flux [54].

In the right-hand panel of Fig. 1 we show the recoil energy spectrum for each neutrino type scattering with a Xenon target. In addition we show the recoil energy spectra for two example WIMPs with masses of 6 GeV and 100 GeV. This is to demonstrate the similarity that certain WIMP masses have with individual neutrino sources. This overlapping between WIMP and neutrino event rates is the reason why neutrinos limit WIMP discovery. For cross sections below the neutrino floor, an experiment which observes an excess in the number of observed events over the expected background cannot determine whether these events were due to a WIMP signal or a statistical fluctuation in the neutrino flux around its systematic uncertainty. Hence the neutrino floor divides the WIMP parameter space into cross sections which induce enough events to be significant over this uncertainty and those which do not.

III. NEUTRINO FLOOR

In this work we draw the neutrino floor for a Xenon target experiment and cut off recoil energies at 3 eV to show its extent down to low WIMP masses. Although this cutoff is much lower than the threshold energies currently achievable it is important to note that the neutrino floor does not correspond to a limit that could be observed by a particular experiment. The neutrino floor is a purely theoretical boundary that depends only on the content of the WIMP and neutrino event rates and is defined without considering any additional experimental effects. The threshold of 3 eV is chosen so that the floor can be mapped at low WIMP masses while excluding pp neutrinos. Importantly, this choice of threshold and target is consistent with other studies of the neutrino floor upon which this work builds: Refs. [5,15,16,18,19,48]. Furthermore, ultralow thresholds are not without experimental motivation; for instance a recent work by Mirabolfathi *et al.* [47] outlined how with current advances in technology, ultralow thresholds down to ~ 10 eV may be achievable in cryogenic detectors with excellent energy resolution. However in the interest of relating studies of the neutrino floor to more realistic projections for future experimental limits we will explore the inclusion of energy resolution, efficiency and a higher energy threshold in Sec. V, aspects which are not usually included in neutrino floor calculations.

To calculate the neutrino floor we adopt a binned likelihood with $N_{\mathrm{bins}} = 100$ to allow us to efficiently perform our analysis with large numbers of neutrino events. The likelihood is written as the product of the Poisson probability distribution function ($\mathcal{P}$) for each bin, multiplied by individual likelihood functions parametrizing the uncertainties on each neutrino flux normalization and each astrophysical parameter,

$$\mathcal{L}(m_\chi, \sigma_{\chi-n}, \Phi, \boldsymbol{\Theta}) = \prod_{i=1}^{N_{\mathrm{bins}}} \mathcal{P}\left(N^i_{\mathrm{obs}} | N^i_\chi + \sum_{j=1}^{n_\nu} N^i_\nu(\phi^j)\right) \times \prod_{j=1}^{n_\nu} \mathcal{L}(\phi^j) \prod_{k=1}^{n_\theta} \mathcal{L}(\theta^k), \tag{5}$$

where $\Phi = \{\phi^1, \ldots, \phi^{n_\nu}\}$ are the neutrino fluxes for each of the n_ν neutrino types and $\boldsymbol{\Theta} = \{\theta^1, \ldots, \theta^{n_\theta}\}$ contains the n_θ astrophysical uncertainties under consideration which will vary depending on the choice of velocity distribution, e.g., the standard halo model: $\boldsymbol{\Theta}_{\mathrm{SHM}} = \{v_0, v_{\mathrm{esc}}, \rho_0\}$. The functions $\mathcal{L}(\phi^j)$ are the Gaussian parametrizations for each neutrino flux (see Table I) and similarly the likelihood functions $\mathcal{L}(\theta^k)$ parametrize the systematic uncertainty on each astrophysical parameter. Inside the Poisson function we have for each bin i, the observed number of events N^i_{obs}, the expected number of WIMP events N^i_χ given by

$$N^i_\chi(m_\chi, \sigma_{\chi-n}, \boldsymbol{\Theta}) = \mathcal{E} \int_{E_i}^{E_{i+1}} \frac{\mathrm{d}R_\chi}{\mathrm{d}E_r} \mathrm{d}E_r, \tag{6}$$

and $N^i_\nu(\phi^j)$ which is the expected number of neutrino events from the jth neutrino species,

$$N^i_\nu(\phi^j) = \mathcal{E} \int_{E_i}^{E_{i+1}} \frac{\mathrm{d}R_\nu}{\mathrm{d}E_r}(\phi^j) \mathrm{d}E_r, \tag{7}$$

where $\mathcal{E}$ is the exposure of the experiment which we will quote in units of ton-years.

Limits placed on the WIMP mass–cross section parameter space by a given experiment can be calculated using

various statistical methods. The approach taken by, for example, Refs. [15,16,19], uses a profile likelihood ratio test statistic to define the neutrino floor as a discovery limit, which is set at the minimum cross section for which a 3σ discovery of a WIMP is possible in 90% of all Monte Carlo realizations. The profile likelihood ratio comprises a hypothesis test between the null hypothesis H_0 (neutrino only) and the alternative hypothesis H_1 which includes both neutrinos and a WIMP signal while incorporating systematic uncertainties, in this case on the flux of each neutrino component Φ and, additionally for this work, astrophysical parameters $\mathbf{\Theta}$. We can then test the background-only hypothesis, H_0, on a simulated data set by attempting to reject it using the likelihood ratio,

$$\lambda(0) = \frac{\mathcal{L}(\sigma_{\chi-n} = 0, \hat{\hat{\Phi}}, \hat{\hat{\mathbf{\Theta}}})}{\mathcal{L}(\hat{\sigma}_{\chi-n}, \hat{\Phi}, \hat{\mathbf{\Theta}})}, \tag{8}$$

where $\hat{\Phi}$, $\hat{\mathbf{\Theta}}$ and $\hat{\sigma}_{\chi-n}$ denote the values of Φ, $\mathbf{\Theta}$ and $\sigma_{\chi-n}$ that maximize the unconditional $\mathcal{L}$ and $\hat{\hat{\Phi}}$ and $\hat{\hat{\mathbf{\Theta}}}$ denote the values of Φ and $\mathbf{\Theta}$ that maximize $\mathcal{L}$ under the condition $\sigma_{\chi-n} = 0$; i.e., we are profiling over the nuisance parameters Φ and $\mathbf{\Theta}$. Note that the test is conducted at fixed WIMP mass and then repeated over a range of input masses. As introduced in Ref. [62], the test statistic q_0 is then defined as

$$q_0 = \begin{cases} -2\ln\lambda(0) & \hat{\sigma}_{\chi-n} > 0, \\ 0 & \hat{\sigma}_{\chi-n} < 0. \end{cases} \tag{9}$$

If a large value of q_0 is calculated then this implies that the alternative hypothesis gives a better fit to the data and the existence of a WIMP signal is preferred. The p-value, p_0, of a particular experiment is the probability of finding a value of the test statistic larger than or equal to the observed value, $q_0^{\rm obs}$, if the null hypothesis is correct,

$$p_0 = \int_{q_0^{\rm obs}}^{\infty} f(q_0|H_0)\mathrm{d}q_0, \tag{10}$$

where $f(q_0|H_0)$ is the probability distribution function of the test statistic under the background-only hypothesis. From Wilks's theorem [62], q_0 asymptotically follows a χ^2 distribution with one degree of freedom and therefore the significance, Z, in units of Gaussian standard deviation (σ) is simply given by $Z = \sqrt{q_0^{\rm obs}}$. The discovery limit for a particular input WIMP mass is then found by finding the smallest input cross section for which 90% of all Monte Carlo evaluations of the test statistic give $Z \geq 3$.

When discussing WIMP and neutrino detection the term "neutrino floor" is loosely applied to the region of WIMP parameter space for which neutrinos become a problematic background. But in fact how this limit evolves as a function of detector exposure is slightly more complex, as we will now briefly discuss. In the case of an experiment which only records the event number, for example a bubble chamber, the minimum discoverable cross section at a given fixed WIMP mass plateaus as the experiment detects an increasing number of events and for large numbers of events there can be no background subtraction. This is due to the systematic uncertainty on the neutrino flux; small cross sections which induce an excess in the number of events less than that due to fluctuations around the expected neutrino flux cannot be attributed to a WIMP with the required significance. One might imagine a hypothetical situation in which the expected neutrino event rate was known with perfect certainty; in this case there would be no limit to how small a cross section the experiment could probe and as the number of background events increased the evolution of the discovery limit is simply set by Poissonian background subtraction. However with a finite systematic uncertainty on each flux component, the neutrino background gives rise to a "floor"—a limit that divides the $m_\chi - \sigma_{\chi-n}$ space into WIMPs which are accessible to the experiment and those which are indistinguishable from neutrinos. This problem persists even with the additional recoil energy information because of the similarity in the spectra of WIMP- and neutrino-induced recoils [16]. However the slight differences in the tails of the neutrino and WIMP event rates allow the two spectra to be distinguished once a sufficient number of events has been detected, usually around the order of $\mathcal{O}(1000)$ events (though the precise number depends on the size of the neutrino flux uncertainty).

Figure 2 shows the full evolution of the discovery limit for a Xenon experiment with an extremely low threshold (0.01 eV) to capture the neutrino floor down to pp neutrino energies for completeness. This is a similar plot to a result of Ref. [16] but here we use updated values for the neutrino fluxes and uncertainties and extend to a lower threshold and to larger exposures. It is important to note however that this figure is merely an illustrative demonstration of each neutrino contribution as exposures of up to 10^7 ton-years are clearly unfeasible. In Fig. 2 we see that the floor moves to lower cross sections as the exposure is increased as one would expect; however it acquires peaks where the WIMP recoil spectrum is mimicked by a given neutrino component. The mass at which a peak appears is dependent on the recoil energy range of the neutrino type. The cross section of the peak and how long the peak remains as exposure is increased depends on the uncertainty on the neutrino flux as well as how well the WIMP recoil event rate is mimicked by the neutrino type [16]. With a smaller uncertainty it takes fewer WIMP events to distinguish them from neutrinos. The most important contribution to the neutrino floor is due to ^{8}B neutrinos which cause the floor to appear at 6 GeV and are within the scope of upcoming direct detection experiments. There are also contributions from

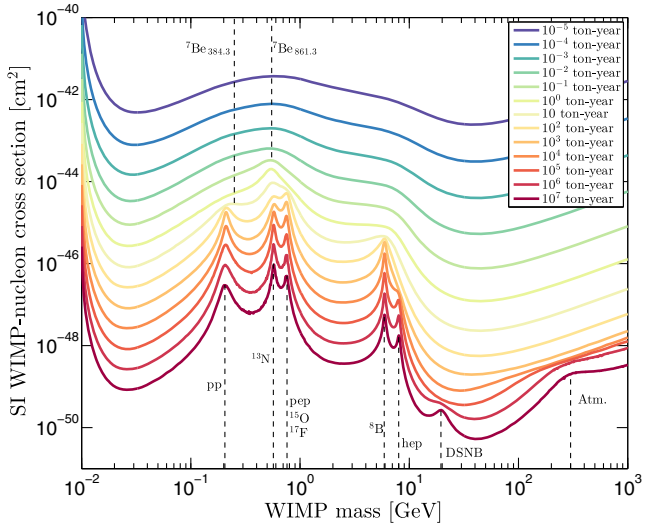

FIG. 2. Illustration of the full dependence of the spin-independent neutrino floor for a Xenon target as a function of WIMP mass and detector exposure, showing the contribution from all sources of neutrino. The neutrino floor has peaks at WIMP masses where the Xenon scattering rate for WIMPs and a certain neutrino source overlap.

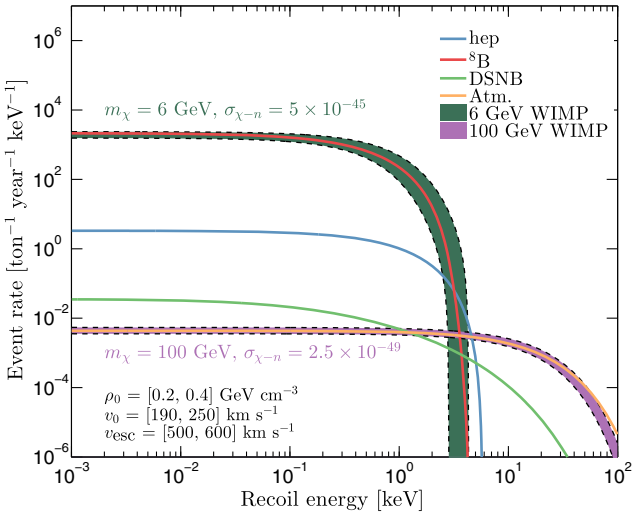

FIG. 3. Spin-independent Xenon elastic scattering rates for 6 and 100 GeV WIMPs and 4 neutrino sources (*hep*, ^{8}B, DSNB and atmospheric neutrinos). The dark green and orange shaded regions respectively refer to the range of scattering rates for 6 and 100 GeV WIMPs with standard halo model parameters taking values between $\rho_0 = [0.2, 0.4]\,\mathrm{GeV\,cm^{-3}}$, $v_0 = [190, 250]\,\mathrm{km\,s^{-1}}$ and $v_{\rm esc} = [500, 600]\,\mathrm{km\,s^{-1}}$.

hep, atmospheric and DSNB neutrinos at higher WIMP masses which may be accessible in very large (> 100 ton) experiments such as DARWIN [63]. Finally, for low WIMP mass searches (below 1 GeV) there is a cluster of peaks due to the lower energy solar neutrinos: *pp*, *pep*, ^{7}Be, ^{15}O, ^{13}N and ^{14}F.

As we are interested in the role played by the astrophysics dependence of the WIMP signal we focus here on low WIMP masses which are the more phenomenologically interesting region. Because light WIMPs probe the tail of the speed distribution, limits in this regime have a greater sensitivity to the values of astrophysical parameters. This choice is also motivated by the fact that advances in technology are more likely to bring about lower threshold detectors (giving access to these low WIMP masses) [47] than allow exposures in excess of 10^6 ton-years to be achieved (which are required to reach the neutrino floor due to atmospheric and diffuse supernovae neutrinos).

IV. ASTROPHYSICAL UNCERTAINTIES

The simplest approximation of a dark matter halo is the standard halo model (SHM): an isotropic and isothermal sphere of dark matter with a $1/r^2$ density profile in which the Milky Way stellar disk is embedded. The velocity distribution of dark matter yielded by such a model has a Maxwell-Boltzmann form and is usually truncated at the escape speed of the Galaxy,

$$f(\mathbf{v}) = \begin{cases} \frac{1}{N} e^{-v^2/v_0^2} & \text{if } |\mathbf{v}| < v_{\rm esc}, \\ 0 & \text{if } |\mathbf{v}| \geq v_{\rm esc}, \end{cases} \tag{11}$$

where $v_{\rm esc}$ is the escape speed, v_0 is the circular rotation speed of the Galaxy and N is a normalization constant found by imposing $\int f(\mathbf{v}) \mathrm{d}^3 v = 1$. Figure 3 shows the energy dependence of the nuclear recoil event rate over a range of input values for the three free parameters of this model: local density ρ_0, circular rotation speed v_0 and escape velocity $v_{\rm esc}$. As mentioned in Sec. III we see that light WIMPs have a greater sensitivity to changes in the astrophysical input than heavier WIMPs and that the most visible change is around the tail of the recoil distribution (around 1 keV for a 6 GeV WIMP for example). We will first consider the effect of each parameter of the SHM individually in Secs. IV A–IV C, as well as the assumption for the speed distribution in Sec. IV D, before combining all sources of uncertainty in Sec. IV E.

A. Escape velocity

The escape velocity is the maximum speed a dark matter particle can have while still being considered gravitationally bound to the Milky Way. It in principle sets the maximum WIMP speed that can be detected on Earth. The escape velocity can be measured directly by finding high velocity stars in the Milky Way to attempt to map the tail of the global Galactic speed distribution [64]. Alternatively it can be inferred by calculating the gravitational potential of the Galaxy using astronomical data. The most noteworthy estimates to date have been made using data from the RAVE survey [65] first released in 2006. An estimate of $v_{\rm esc} = 544^{+65}_{-46}\ \mathrm{km\,s^{-1}}$ [66] was made using the first release of this data and is commonly used to derive many direct

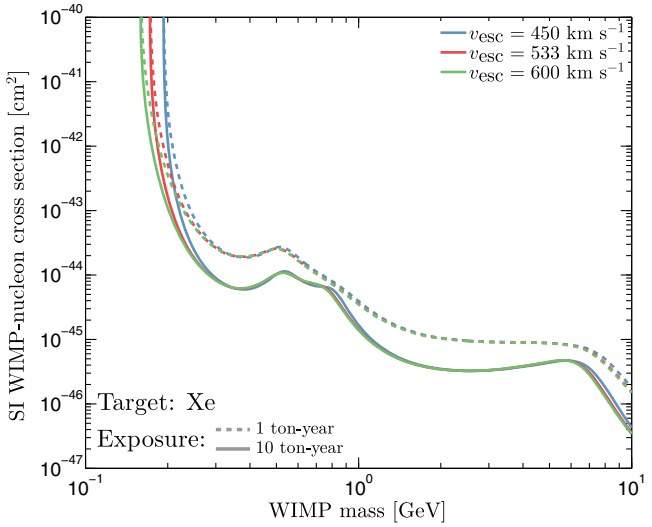

FIG. 4. Spin-independent neutrino floor for a Xenon experiment with different values of input escape velocity. The dashed lines are for a 1 ton-year exposure and the solid lines for a 10 ton-year exposure. The blue, red and green colors correspond to input escape velocities of 450, 533 and 600 km s^{-1} respectively.

detection exclusion limits, but the most recent estimate from 2014 based on the fourth release of RAVE data finds $v_{esc} = 533^{+54}_{-41}$ km s^{-1} [67].

Since the escape velocity can only control the tail of the recoil distribution and because the speed distribution is very small at its tail, the effect of changing the speed at which it is truncated only has a small effect on the overall shape of the recoil energy spectrum. Figure 4 shows the neutrino floor for three values of the escape velocity. We can see here that changing the escape velocity has a very marginal effect on the overall shape of the neutrino floor. The most noticeable effect is around 0.2 GeV where the limits sharply increase due to the maximum energy recoils falling below 3 eV. For smaller values of escape velocity this sharp increase in the discovery limit appears at larger WIMP masses. This is not strictly a feature of the neutrino floor but an artifact of the calculation being performed with a finite energy threshold. There are some slight differences in the floors around 0.8 GeV and 8 GeV however for the different values of v_{esc} shown here and they are largely indistinguishable.

It should be noted that the values of escape velocity chosen in Fig. 4 cover a wider range than the expected uncertainty in the central value of 533 km s^{-1} so given these results we deduce that including the uncertainty in v_{esc} will only have a small effect. When in subsequent results (Sec. IV E) we include uncertainties in the statistical analysis, we will use the central RAVE value and a range of uncertainties up to the values quoted in the literature.

B. Solar velocity

The velocity distribution is observed through a Galilean boost into the laboratory frame by the velocity of the Earth relative to the halo, $\mathbf{v}_{lab}$. This velocity is the sum of four components: the bulk velocity of the Milky Way local standard of rest (LSR) $\mathbf{v}_0$, the peculiar velocity of the Sun with respect to the LSR $\mathbf{v}_\odot$, the velocity of the Earth with respect to the Sun $\mathbf{v}_{rev}$, and the rotation of the Earth $\mathbf{v}_{rot}$. The latter two velocities are responsible for the annual [45] and diurnal [68] modulations in the event rate respectively and are known theoretically with effectively perfect precision. The peculiar velocity is believed to possess a reasonably small uncertainty. A value commonly used from Schoenrich *et al.* [69] gives $\mathbf{v}_\odot = (11.1, 12.24, 7.25)$ km s^{-1} in Galactic coordinates with roughly 1 km s^{-1} sized systematic errors. In this section we will ignore these contributions to the laboratory velocity; however when we incorporate the time dependencies of the WIMP and solar neutrino event rates in Sec. VII the Earth's revolution and rotation velocities will be included.

The largest source of uncertainty in the laboratory velocity comes from the Sun's circular speed. It is also the largest contribution to $\mathbf{v}_{lab}$ at roughly $v_0 \sim 220$ km s^{-1} which is the fiducial value usually used [70]. The circular speed has been measured in various ways; for instance measurements of the proper motions of objects such as nearby stars or Sgr A* located at the Galactic center can be used to constrain the quantity $(v_0 + V_\odot)/R_\odot$ where $V_\odot$ is the second component of $\mathbf{v}_\odot$ and $R_\odot$ is the solar Galactic radius. Given independent constraints on the Sun's peculiar velocity and radius one can combine measurements to arrive at a constraint on v_0. However, as noted by Lavalle and Magni [71] because these estimates depend upon the prior assumptions made about other parameters, combining measurements of, for instance, $R_\odot$ and $V_\odot$ from different

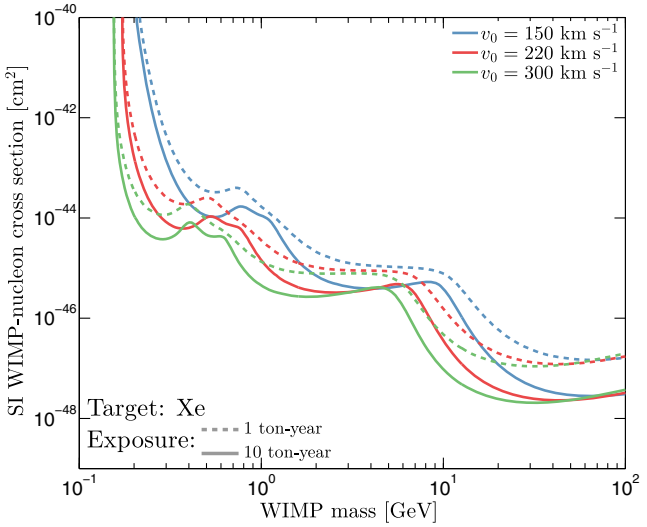

FIG. 5. Spin-independent neutrino floor for a Xenon experiment with different values of input circular velocity v_0. The dashed lines are for a 1 ton-year exposure and the solid lines for a 10 ton-year exposure. The blue, red and green colors correspond to an input v_0 of 150, 220 and 300 km s^{-1} respectively.

sources may lead to spurious resulting values and underestimated errors. Reference [72] however contains an estimate for v_0 of 243 ± 6 km s^{-1} which makes use of the same priors on solar motion as the study based on the RAVE data (Ref. [69]), meaning its value is consistent with $v_{\rm esc} = 533$ km s^{-1}.

Given the discrepancies between astronomically observed values for v_0, both with each other and with the fiducial value of 220 km s^{-1}, we will be pessimistic about our chosen uncertainty on v_0. Figure 5 shows the neutrino floor for a range of values of v_0, keeping other parameters constant. Comparing with Fig. 4 we can see the effect of v_0 is much more noticeable. Whereas $v_{\rm esc}$ affects only the tail of the recoil energy distribution, v_0 affects the entirety. As explained in Sec. III, the shape of the neutrino floor is determined by the WIMP masses which scatter into energies that overlap with each neutrino component. For smaller values of v_0 larger WIMP masses are needed to produce recoils which are mimicked by the same neutrino type; it is understandable then that for smaller v_0, the neutrino floor is shifted to higher WIMP masses.

C. Local density

The local density of WIMPs ρ_0 is most often taken to be its fiducial value of 0.3 GeV cm^{-3}. This is mostly because it appears as a multiplicative factor in the WIMP event rate and is as a result degenerate with the scattering cross section. Moreover, calculations of the local density have been historically variable. Recent work by Ref. [73] finds a value of 0.542 ± 0.042 GeV cm^{-3} using a host of red clump stars from RAVE observations, whereas Ref. [71] finds values between 0.42 and 0.08 depending on the choice of prior on v_0. For this study however the effect of changing local density is straightforward; a larger value of ρ_0 simply shifts the floor to smaller cross sections by the same factor.

D. Speed distribution

Most direct detection analyses use the SHM Maxwellian speed distribution both for simplicity and to establish a baseline to compare different experiments (given that there is no fully agreed upon alternative). There have been numerous attempts to find empirical fitting functions to better capture the phase space structure found in N-body and hydrodynamic simulations [27,74–78] as well as parametrizations that decompose the speed or velocity distribution in an astrophysics-independent way [79,80]. Some studies of data from hydrodynamic simulations suggest that the SHM is a satisfactory approximation to the Milky Way once baryons are taken into account (e.g., Ref. [77]); however others such as Sloane *et al.* [78] claim that the SHM overpredicts the amount of dark matter in the tail and hence gives overly optimistic discovery limits. To address these concerns, and because when discriminating between WIMPs and neutrinos the high speed tail of the distribution is especially important, we show discovery limits for a range of different models. Here we describe three examples that we use to serve as a demonstration of the effect of the input speed distribution on the neutrino floor. These cover a reasonable range of possible parametrizations with the exception of speed distributions that contain additional features such as tidal streams which we leave for future work.

Halos with double power law density profiles, such as the NFW profile, can have their high velocity dependence better reproduced if a distribution is chosen of the form [81],

$$f_{\rm DPL}(\mathbf{v}) = \begin{cases} \frac{1}{N}\left[\exp\left(-\frac{v_{\rm esc}^2 - v^2}{k v_0^2}\right) - 1\right]^k & \text{if } |\mathbf{v}| < v_{\rm esc}, \\ 0 & \text{if } |\mathbf{v}| \geq v_{\rm esc}. \end{cases} \tag{12}$$

This model is a modification of the SHM [the form of Eq. (11) is recovered when setting $k = 1$]. Results from N-body simulations suggest k to be in the range $1.5 < k < 3.5$ [74,82].

In Ref. [75] it was found that the Tsallis model produced a better fit to simulations which included baryons. It involves a speed distribution of the form,

$$f_{\rm Tsallis}(\mathbf{v}) = \begin{cases} \frac{1}{N}\left[1 - (1-q)\frac{v^2}{v_0^2}\right]^{1/(1-q)} & \text{if } |\mathbf{v}| < v_{\rm esc}, \\ 0 & \text{if } |\mathbf{v}| \geq v_{\rm esc}, \end{cases} \tag{13}$$

with best fit parameters of $q = 0.773$, $v_0 = 267.2$ km s^{-1} and $v_{\rm esc} = 560.8$ km s^{-1}.

The final speed distribution we consider is one introduced by Mao *et al.* [27,83], which was found to improve the fit in simulations. It takes a form characterized by an index p,

$$f_{\rm Mao}(\mathbf{v}) = \begin{cases} \frac{1}{N} e^{-v/v_0}(v_{\rm esc}^2 - v^2)^p & \text{if } |\mathbf{v}| < v_{\rm esc}, \\ 0 & \text{if } |\mathbf{v}| \geq v_{\rm esc}, \end{cases} \tag{14}$$

where results from the Rhapsody and Bolshoi simulations give p in the range $0 < p < 3$.

The neutrino floor obtained under the assumption of these alternative distributions is shown in Fig. 6. When the underlying speed distribution is changed the position of the floor shifts only very slightly: shifting to slightly higher WIMP mass for the double power law and Mao models and to slightly smaller WIMP masses for the Tsallis model. Hence for this reason, and in the interest of efficiency, from here we will neglect the dependence on the speed distribution and focus our attention on the SHM.

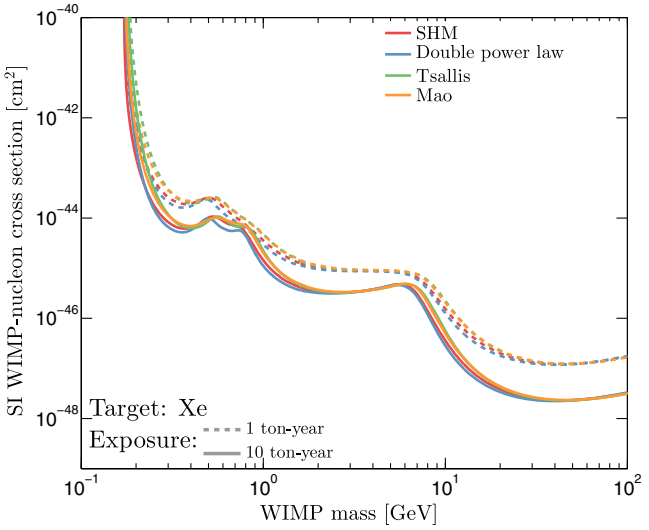

FIG. 6. Spin-independent discovery limit for a Xenon experiment for different input speed distributions. The dashed lines are for a 1 ton-year exposure and the solid lines for a 10 ton-year exposure. The blue, green and orange colors correspond to the double power law, Tsallis and Mao distributions respectively. The red lines are for the SHM with $v_0 = 220\ \mathrm{km\,s^{-1}}$ and $v_{\mathrm{esc}} = 533\ \mathrm{km\,s^{-1}}$.

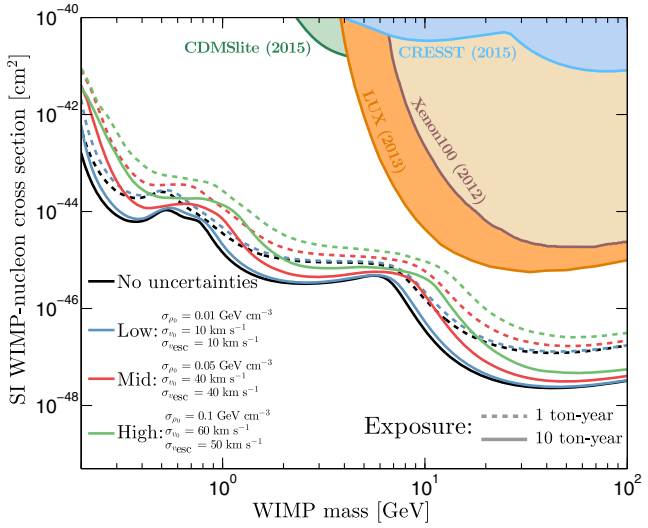

FIG. 7. Spin-independent neutrino floor as a function of WIMP mass calculated with the inclusion of astrophysical uncertainties in the profile likelihood analysis. The dashed lines are for an exposure of 1 ton-year and the solid lines are for an exposure of 10 ton-years. The blue, red and green curves correspond to three sets of values of the 1σ uncertainty on the parameters ρ_0, v_0 and v_{esc} displayed in the figure and the text. The size of the uncertainties are labeled from low to high with values indicated. The filled regions are currently excluded by experiments, CRESST [84], CDMSlite [85], Xenon100 [6] and LUX [7].

E. Neutrino floor with uncertainties

Now that we have demonstrated the effect of each parameter individually on the neutrino floor we now unfix the astrophysics parameters in the profile likelihood ratio test and account for their uncertainty with a multiplicative Gaussian parametrization. Figure 7 shows the discovery limits as a function of the width of the Gaussian uncertainty in each parameter. We label the sets of the uncertainty values "low," "mid" and "high." The low values for the 1σ uncertainty on ρ_0, v_0 and v_{esc} are respectively, $0.01\ \mathrm{GeV\,cm^{-3}}$, $10\ \mathrm{km\,s^{-1}}$ and $10\ \mathrm{km\,s^{-1}}$. The mid values are $0.05\ \mathrm{GeV\,cm^{-3}}$, $40\ \mathrm{km\,s^{-1}}$ and $40\ \mathrm{km\,s^{-1}}$. And for the high values we use $0.1\ \mathrm{GeV\,cm^{-3}}$, $60\ \mathrm{km\,s^{-1}}$ and $50\ \mathrm{km\,s^{-1}}$.

With the values of the astrophysical parameters uncertain, the experiment is less powerful and the neutrino floor appears at larger cross sections because the WIMP signal becomes saturated with fewer events. We also find that the maxima that appear in the discovery limit due to each neutrino component become broader with the inclusion of uncertainties. As shown in the previous section for different values of v_0 and v_{esc}, the peak in the discovery limit shifts to WIMP masses with recoil energies more closely matching that of the relevant neutrino. Hence, the larger the uncertainty on v_0 and v_{esc} the broader the peak becomes due to the greater allowed range of WIMP masses whose recoils overlap with neutrinos. For instance the peak due to ^{8}B neutrinos now extends up to 15 GeV for the largest set of astrophysical uncertainties.

This result shows that the astrophysical input to the predicted WIMP event rate must be well understood if one wishes to interpret how neutrinos play a role in the discoverability of certain regions of the WIMP mass–cross section parameter space. Particularly this will be a concern for the next generation of direct detection experiments which are set to make limits that come very close to the neutrino bounds calculated in this work which represent a best-case scenario with no additional experimental complications included. In fact as we can see in Fig. 7, the limits we have calculated for the high values of uncertainty come extremely close, down to a factor of 3, to the existing LUX limit just above 10 GeV. Hence we can conclude that unless there are improvements in the knowledge of the astrophysics parameters or the uncertainties on the neutrino flux, the neutrino floor will be encountered by direct detection experiments much sooner than previously thought.

V. FUTURE DETECTORS

Future direct detection experiments such as SuperCDMS [8], Xenon1T [10] and LZ [11] are poised to make the first detection of CNS. In this work so far we have only shown neutrino floor limits which are defined without the consideration of any additional experimental effects. However the neutrino floor limit does not reflect a discovery limit that will be observed directly by any future experiment. In practice all detectors suffer from complications such as

imperfect energy resolution and efficiency, and they have thresholds in the $\mathcal{O}(1\text{–}10)$ keV range as opposed to the ultralow thresholds that are used when calculating the low WIMP mass neutrino floor.

We showed in the previous section that the inclusion of astrophysical uncertainties both raises the cross section of the neutrino floor and extends the range of WIMP masses at which discovery is most prohibited by solar neutrino backgrounds. Given this result, and in the interest of relating the purely theoretical neutrino floor to more realistic projections for future discovery limits we will now include the aforementioned experimental effects in a neutrino + WIMP analysis, with the same astrophysical uncertainties introduced in Sec. IV.

The energy resolution is taken into account by convolving the event rate with a Gaussian resolution function defined by an energy-dependent resolution $\sigma(E_r)$,

$$\frac{\mathrm{d}R}{\mathrm{d}E_r}(E_r) = \int_0^\infty \frac{1}{\sqrt{2\pi}\sigma(E_r)} e^{-\frac{(E_r-E_r')^2}{2\sigma^2(E_r)}} \frac{\mathrm{d}R}{\mathrm{d}E_r}(E_r')\mathrm{d}E_r'. \quad (15)$$

The results we will show in this section are for a 2 keV threshold Xenon detector with a 10 ton target mass over 1000 days running time, which is a reasonable estimate to the specifications of near-future and beyond experiments such as LZ and Xenon1T. The energy resolution we take to be a constant 80% at 1σ over the full energy range, i.e. $\sigma(E_r) = 0.8E_r$. We also take into account the efficiency of the detector which decreases towards the threshold of the experiment. In the following results we assume a simple efficiency curve (similar but less optimistic than in Ref. [50]) which increases linearly from 25% at the threshold energy to 100% at the maximum energy of 50 keV. Figure 8 shows the discovery limit for this detector when neutrinos and astrophysical uncertainties are included. We show results for three sets of values of the uncertainties and the discovery limits for this more realistic mock detector compared with the neutrino floor for each set of uncertainty values.

The results of Fig. 8 follow from those of Fig. 7: when the uncertainty on v_0 is larger, the floor appears at larger WIMP masses for the same reasons as discussed in Sec. IV. In this case we see that for the largest uncertainties the discovery limits lie extremely close to the currently excluded region by LUX. However distinct from the existing excluded regions, the discovery limits shown here are beginning to be limited by the presence of $\sim$150 ^{8}B neutrino events. The discoverable regions are also limited by the loss of information due to the smearing by the energy resolution as well as the loss in numbers of events close to the threshold due to the efficiency of the detector. This means that these limits do not yet approach the neutrino floor limit calculated previously. However the general conclusion of Sec. IV remains, that larger uncertainty values on the astrophysics content of the WIMP signal weaken the possible constraints that can be made by a future experiment.

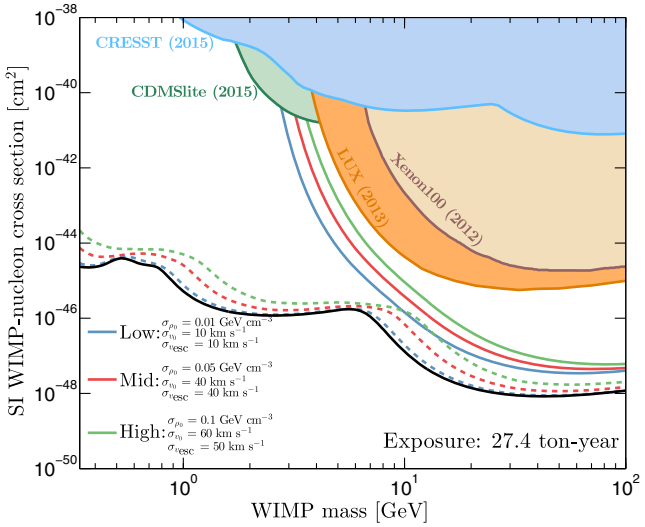

FIG. 8. Spin-independent WIMP-nucleon cross section discovery limit as a function of WIMP mass for three sets of values of the uncertainty placed on the astrophysical parameters: local density, solar velocity and escape velocity. The blue, red and green curves correspond to low, medium and high values for these uncertainties with 1σ values shown. The solid lines are obtained when the detector efficiency is taken into account and the recoil spectrum is convolved with a Gaussian energy resolution with $\sigma(E_r) = 0.8E_r$. The corresponding neutrino floors, i.e., with no detector effects, are shown as dashed lines. The filled regions are currently excluded by experiments, CRESST [84], CDMSlite [85], Xenon100 [6] and LUX [7]. For comparison we show the neutrino floor calculated without considering astrophysical uncertainties, indicated by the black line.

VI. PARAMETER CONSTRAINTS

The goal of this section is to demonstrate the effect neutrino backgrounds have on the measurement of WIMP parameters. The neutrino floor as derived in the previous section is a convenient way of showing how much of the WIMP mass–cross section parameter space is accessible to an ideal experiment. However this limit gives us no information with regards to how the ingredient parameters of the WIMP signal may be constrained, which is undoubtedly a goal of direct detection experiments.

The procedure we call parameter reconstruction is performed by generating mock data covering a range of input WIMP masses and cross sections and then attempting to recover those input parameters with a Bayesian fit. We make use of nested sampling algorithms provided by the MultiNest package [86–88] to explore the likelihood function as described in Sec. III. A summary of the MultiNest input specification and the priors used on each parameter is given in Table II. Note that as we are interested here solely in the effects of adding neutrinos and astrophysical uncertainties

TABLE II. Input specification and priors used for Bayesian parameter estimation using MultiNest.

MultiNest	$N_{\rm live}$	2000	
	Tol	0.001	
	Eff	0.3	
Priors	m_χ	Log-flat	[0.1,1000] GeV
	$\sigma_{\chi-n}$	Log-flat	$[10^{-50}, 10^{-40}]$ cm^2
	ρ_0	Gaussian	0.3 ± 0.1 GeV cm^{-3}
	v_0	Gaussian	220 ± 25 km s^{-1}
	$v_{\rm esc}$	Gaussian	533 ± 47 km s^{-1}
	ϕ_ν^j	Gaussian	[See Table I]

on parameter measurements, we revert to the idealized mock experiments used in Sec. IV so that these effects are clearer.

In Fig. 9 we show the 68% profile likelihood error in the reconstructed values of WIMP mass and cross section, $m_\chi^{68\%}$ and $\sigma_{\chi-n}^{68\%}$. We show how this error varies over a range of input WIMP masses, focusing on light WIMPs in the range 0.2–20 GeV. In each case the input cross section is chosen to produce a fixed number of WIMP events ($N_\chi = 500$, 2500 or 5000 in a 10 ton-year exposure). The lines of constant WIMP event numbers shown in Fig. 9 are chosen so that they fall either above or below the corresponding neutrino floor. For instance the line for $N_\chi = 500$ (green filled region) falls just above the neutrino floor over the full range of WIMP masses, the line corresponding to $N_\chi = 2500$ (red filled region) falls below the floor around 0.6 GeV but above at 6 GeV and the $N_\chi = 5000$ case (blue filled region) falls below the floor around 0.6 GeV and 6 GeV. We can see that the input WIMP parameters which lie below the neutrino floor are very poorly reconstructed with 68% intervals lying outside of the displayed range. However input WIMP parameters above the neutrino floor are reconstructed very well. For input values which lie on the neutrino floor at 6 GeV when the ^{8}B neutrinos mimic the WIMP signal there is a sharp increase in the error on the reconstructed mass and cross section.

In the right-hand panel of Fig. 9 we show the results for the same analysis as in the left-hand panel but now with the astrophysical parameters unfixed in the Bayesian reconstruction. For each set of WIMP input parameters

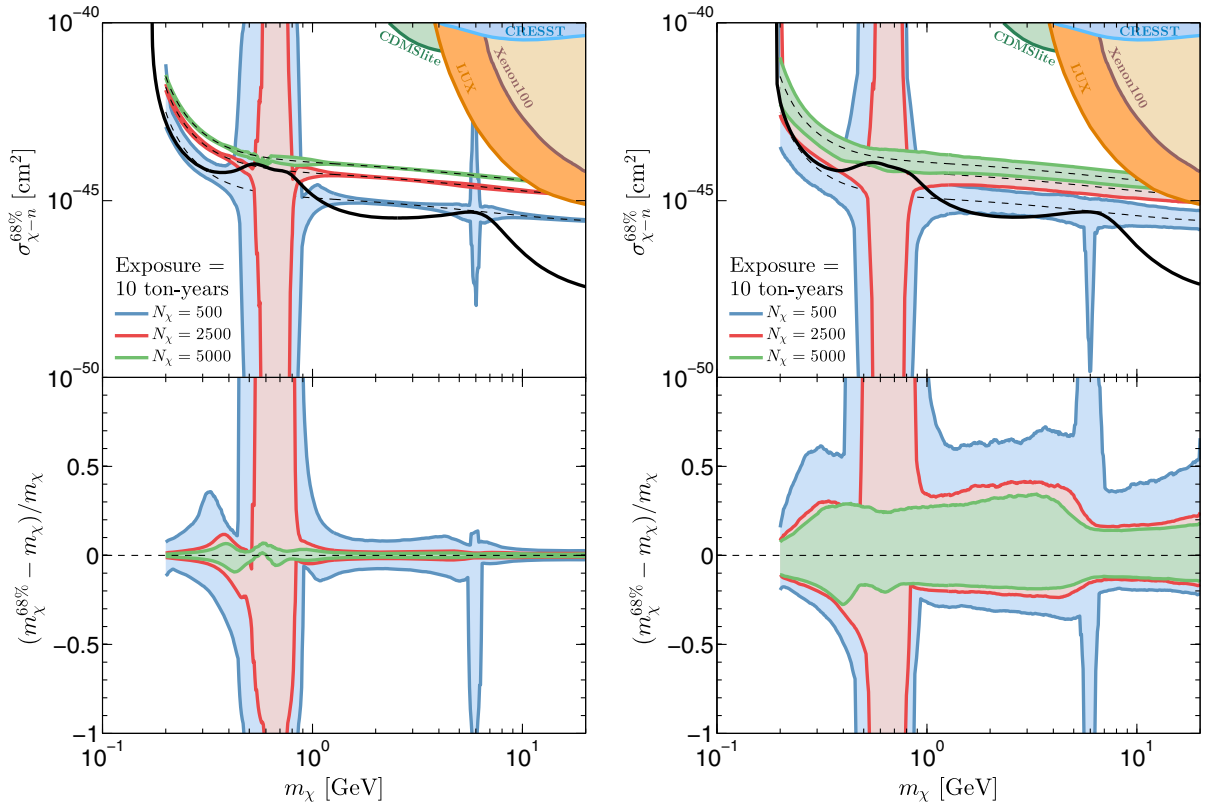

FIG. 9. Left: Errors on the reconstructed values of $\sigma_{\chi-n}$ and m_χ as a function of input WIMP mass in the presence of the neutrino background. The shaded regions enclose the 68% profile likelihood errors on cross section $\sigma_{\chi-n}^{68\%}$ (top panel) and WIMP mass $m_\chi^{68\%}$ (bottom panel, scaled by the input mass m_χ). The input cross section for each WIMP mass is chosen to fix the expected number of WIMP events to 500 (blue), 2500 (red) or 5000 (green). The dashed lines in each region indicate those input values. Right: As in the left panel but with v_0, $v_{\rm esc}$ and ρ_0 allowed to vary. The filled regions are currently excluded by experiments, CRESST [84], CDMSlite [85], Xenon100 [6] and LUX [7].

we see a large increase in the error on their recovered values across the WIMP mass range. We can attribute the increase in error on $\sigma_{\chi-n}$ to the additional uncertainty brought about by the parameter ρ_0, with which it is degenerate. The increase in the m_χ error is largely due to the uncertainty on v_0 which in particular leads to a huge increase in reconstruction error around 6 GeV for the case when $N_\chi = 500$. Following the conclusion of Sec. IV E which found that accounting for astrophysical uncertainties prohibited a larger range of WIMP parameter values from being accessed, similarly here the inclusion of astrophysical uncertainties has a detrimental effect on the measurement of those parameter values. It is well known that a good understanding of the astrophysics dependence of the WIMP signal is crucial for making measurements of WIMP properties; however we have shown here that this is especially true when neutrinos are the dominant background.

VII. INCLUDING TIME INFORMATION

It was shown in Ref. [17] that the time dependence of the WIMP and solar neutrino event rates provides a distinguishing feature between the two signals which can help circumvent the neutrino floor with fewer events than a recoil-energy-only analysis. The WIMP signal is time dependent because of a well-known annual modulation effect due to the motion of the Earth with respect to the Sun [45]. We can insert this time dependence into the WIMP calculation by simply including the additional velocity $\mathbf{v}_{\mathrm{EarthRev}}(t)$ in the lab velocity $\mathbf{v}_{\mathrm{lab}}$. Details on the time dependence of this velocity component can be found in Ref. [68].

The solar neutrino flux also exhibits an annual modulation due to the eccentricity of the Earth's orbit. The time dependence can be written as

$$\frac{\mathrm{d}\Phi(t)}{\mathrm{d}E_\nu} = \frac{\mathrm{d}\Phi}{\mathrm{d}E_\nu}\left[1 + 2\epsilon\cos\left(\frac{2\pi(t-t_\nu)}{T_\nu}\right)\right], \tag{16}$$

where t is the time from January 1, $\epsilon = 0.016722$ is the eccentricity of the Earth's orbit, $t_\nu = 3$ days is the time at which the Earth-Sun distance is shortest (and hence the solar neutrino flux is largest) and $T_\nu = 1$ year. Both the solar neutrino and WIMP event rates have a ~5% annual modulation but with a 5 month phase difference.

We now extend to an energy + time analysis by replacing the likelihood of Eq. (5) with

$$\mathcal{L}(m_\chi, \sigma_{\chi-n}, \Phi, \boldsymbol{\Theta}) = \prod_{i=1}^{N_{E_r}}\prod_{j=1}^{N_t}\mathcal{P}\left(N^i_{\mathrm{obs}}|N^i_\chi + \sum_{j=1}^{n_\nu} N^{ij}_\nu(\phi^k)\right) \times \prod_{k=1}^{n_\nu}\mathcal{L}(\phi^k)\prod_{l=1}^{n_\theta}\mathcal{L}(\theta^l), \tag{17}$$

where we now bin in both energy and time with N_{E_r} and N_t bins respectively. The number of WIMP events in bin (i, j) is

$$N^{ij}_\chi(m_\chi, \sigma_{\chi-n}, \boldsymbol{\Theta}) = \mathcal{M}\int_{E_i}^{E_{i+1}}\int_{t_j}^{t_{j+1}}\frac{\mathrm{d}R_\chi(t)}{\mathrm{d}E_r}\mathrm{d}t\mathrm{d}E_r, \tag{18}$$

and $N^{ij}_\nu(\phi^k)$ is the number of expected neutrino events from the kth neutrino species,

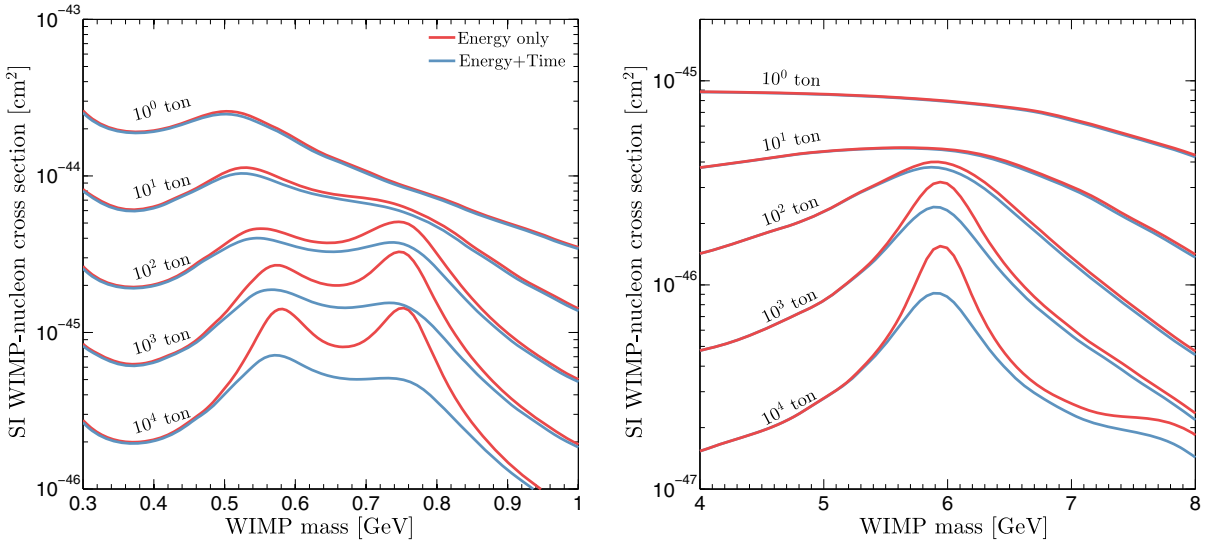

FIG. 10. Spin-independent WIMP-nucleon neutrino floor evolution in the 0.3–1 GeV (left) and 4–5 GeV mass range (right). The red curves show the bounds obtained when only energy information is considered and the blue curves show the improvement when time information is added. There are four sets of curves shown for four detector masses from 1 ton to 10^4 tons (top to bottom). In each case the exposure time was kept at a constant 1 year from January 1, 2016.

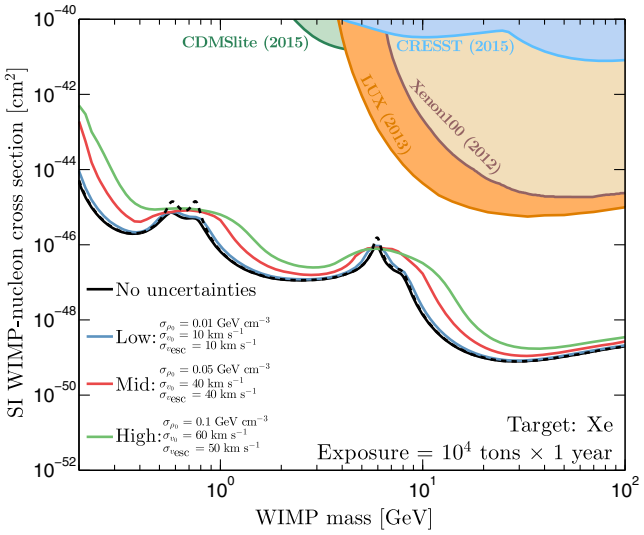

FIG. 11. Spin-independent neutrino floor as a function of WIMP mass calculated with the inclusion of astrophysical uncertainties and time dependence. The blue, red and green curves correspond to 3 sets of 1σ uncertainties on the parameters ρ_0, v_0 and $v_{\rm esc}$. The sizes of the uncertainties are labeled from low to high with values indicated. The black lines are the energy-information-only neutrino floor (dashed black line) and the energy + time information neutrino floor (solid black line). The filled regions are currently excluded by experiments, CRESST [84], CDMSlite [85], Xenon100 [6] and LUX [7].

$$N_\nu^{ij}(\phi^k) = \mathcal{M}\int_{E_i}^{E_{i+1}}\int_{t_j}^{t_{j+1}}\frac{\mathrm{d}R_\nu(t)}{\mathrm{d}E_r}(\phi^k)\mathrm{d}t\mathrm{d}E_r, \quad (19)$$

where $\mathcal{M}$ is the mass of the detector.

In Fig. 10 we show the improvement on the neutrino floor limit under the inclusion of time information. We show only narrow mass ranges: between 0.3 and 1 GeV when the ^{7}Be, *pep*, ^{13}N, ^{15}O and ^{17}F neutrinos play the biggest role and between 4 and 8 GeV when the floor is induced by ^{8}B and *hep* neutrinos. Outside of these specific mass ranges (for the exposures considered here) the improvement offered by time information is negligible. Because the annual modulation amplitudes are small, obtaining a benefit from time information needs in excess of $\mathcal{O}(1000)$ neutrino events. Here, to isolate the effects of including time information in the neutrino floor calculation, we have neglected additional detector effects and use a 3 eV energy cutoff to map the low WIMP mass dependence.

Incorporating uncertainties on the SHM parameters into the energy + time analysis we obtain limits shown in Fig. 11. These limits are analogous to those of Fig. 7 extended to an exposure large enough to receive the benefit of time information (10^4 ton-years). Again the discovery limit under the assumption of the largest values of uncertainty is up to an order of magnitude higher than the astrophysics fixed case around 15 GeV. However it still remains below the energy-only limit around the peaks due to the solar neutrino contributions meaning the inclusion of time information still mitigates the neutrino background even when astrophysical uncertainties are taken into account.

VIII. SUMMARY

In this work we have demonstrated the impact of astrophysics uncertainties on the calculation of the neutrino floor. Relaxing the assumption of perfectly known astrophysics parameters such as the solar velocity, escape speed and local WIMP density results in a shift in the range of WIMP parameter values that are prohibited by the neutrino background. We find that if there are reasonably large uncertainties in the various astrophysics parameters (close to those currently known) then the neutrino floor extends to larger WIMP masses and is closer to existing experimental limits than previously thought.

When attempting to reconstruct the input WIMP and neutrino parameters we find that unfixing the astrophysics parameters induces a significant increase in the uncertainty of the reconstruction. Input WIMP parameters that lie below the neutrino floor are recovered extremely poorly, and this problem is only worsened by the inclusion of astrophysical uncertainties; both the errors on the recovered values of m_χ and $\sigma_{\chi-n}$ are increased but the range of masses for which the reconstruction fails also increases. This means that even if experiments were to become sensitive to a WIMP with cross section and mass close to the neutrino floor then the measurement of the properties of such a WIMP will be extremely difficult or impossible to measure accurately in conjunction with astrophysical parameters.

The first detection of coherent neutrino-nucleus scattering is expected to be made with the forthcoming generation of ton-scale direct detection experiments [11]. When this occurs it will be crucial to begin to implement strategies for dealing with neutrino backgrounds. This can be achieved in a number ways. As can be seen in this work, as well as that of Ref. [17] the number of events observed at these detector masses are not yet enough to utilize the time dependence of the WIMP and neutrino signals to discriminate the two. For spin-dependent interactions as well as nonrelativistic effective field theory operators, complementarity between target materials will be a powerful and relatively easy method for discriminating neutrinos [16,21]. Independent of the WIMP-nucleus interaction however, directional detection, if experimentally feasible, will prove the most powerful scheme for distinguishing WIMPs and neutrinos [18–20]. The angular signatures of WIMP and neutrino recoils are entirely distinct and this is true for any relationship set of astrophysical inputs or WIMP-nucleus interactions. However for the upcoming generation of direct detection experiments which will lack sensitivity to either direction or time dependence, we have shown that

a better understanding of the uncertainty in the astrophysical dependence of a predicted WIMP signal will be vital to understand in order to deal with the neutrino background.

ACKNOWLEDGMENTS

The author thanks Anne M. Green for helpful discussion and comments on the manuscript. The author is supported by the Science & Technology Facilities Council (STFC).

[1] P. A. R. Ade *et al.* (Planck Collaboration), Planck 2015 results. XIII. Cosmological parameters, arXiv:1502.01589.
[2] M. W. Goodman and E. Witten, Detectability of certain dark matter candidates, Phys. Rev. D **31**, 3059 (1985).
[3] G. Jungman, M. Kamionkowski, and K. Griest, Supersymmetric dark matter, Phys. Rep. **267**, 195 (1996).
[4] G. Bertone, D. Hooper, and J. Silk, Particle dark matter: Evidence, candidates and constraints, Phys. Rep. **405**, 279 (2005).
[5] J. Monroe and P. Fisher, Neutrino backgrounds to dark matter searches, Phys. Rev. D **76**, 033007 (2007).
[6] E. Aprile *et al.* (XENON100 Collaboration), Dark Matter Results from 225 Live Days of XENON100 Data, Phys. Rev. Lett. **109**, 181301 (2012).
[7] D. S. Akerib *et al.* (LUX Collaboration), First Results from the LUX Dark Matter Experiment at the Sanford Underground Research Facility, Phys. Rev. Lett. **112**, 091303 (2014).
[8] R. Agnese *et al.* (SuperCDMS Collaboration), Search for Low-Mass Weakly Interacting Massive Particles with SuperCDMS, Phys. Rev. Lett. **112**, 241302 (2014).
[9] T. Marrodan Undagoitia and L. Rauch, Dark matter direct-detection experiments, J. Phys. G **43**, 013001 (2016).
[10] E. Aprile *et al.* (XENON Collaboration), Physics reach of the XENON1T dark matter experiment, J. Cosmol. Astropart. Phys. 04 (2016) 027.
[11] D. S. Akerib *et al.* (LZ Collaboration), LUX-ZEPLIN (LZ) conceptual design report, arXiv:1509.02910.
[12] B. Cabrera, L. M. Krauss, and F. Wilczek, Bolometric Detection of Neutrinos, Phys. Rev. Lett. **55**, 25 (1985).
[13] L. E. Strigari, Neutrino coherent scattering rates at direct dark matter detectors, New J. Phys. **11**, 105011 (2009).
[14] A. Gutlein, C. Ciemniak, F. von Feilitzsch, N. Haag, M. Hofmann, C. Isaila, T. Lachenmaier, J.-C. Lanfranchi, L. Oberauer, and S. Pfister, Solar and atmospheric neutrinos: Background sources for the direct dark matter search, Astropart. Phys. **34**, 90 (2010).
[15] J. Billard, L. Strigari, and E. Figueroa-Feliciano, Implication of neutrino backgrounds on the reach of next generation dark matter direct detection experiments, Phys. Rev. D **89**, 023524 (2014).
[16] F. Ruppin, J. Billard, E. Figueroa-Feliciano, and L. Strigari, Complementarity of dark matter detectors in light of the neutrino background, Phys. Rev. D **90**, 083510 (2014).
[17] J. H. Davis, Dark matter vs. neutrinos: The effect of astrophysical uncertainties and timing information on the neutrino floor, J. Cosmol. Astropart. Phys. 03 (2015) 012.
[18] P. Grothaus, M. Fairbairn, and J. Monroe, Directional dark matter detection beyond the neutrino bound, Phys. Rev. D **90**, 055018 (2014).
[19] C. A. J. O'Hare, A. M. Green, J. Billard, E. Figueroa-Feliciano, and L. E. Strigari, Readout strategies for directional dark matter detection beyond the neutrino background, Phys. Rev. D **92**, 063518 (2015).
[20] T. Franarin and M. Fairbairn, Reducing the solar neutrino background using polarised helium-3, Phys. Rev. D **94**, 053004 (2016).
[21] J. B. Dent, B. Dutta, J. L. Newstead, and L. E. Strigari, No ν floors: Effective field theory treatment of the neutrino background in direct dark matter detection experiments, Phys. Rev. D **93**, 075018 (2016).
[22] M. Persic, P. Salucci, and F. Stel, The universal rotation curve of spiral galaxies: 1. The dark matter connection, Mon. Not. R. Astron. Soc. **281**, 27 (1996).
[23] A. Klypin, H. Zhao, and R. S. Somerville, Lambda CDM-based models for the Milky Way and M31 I: Dynamical models, Astrophys. J. **573**, 597 (2002).
[24] L. E. Strigari, Galactic searches for dark matter, Phys. Rep. **531**, 1 (2013).
[25] M. Vogelsberger, A. Helmi, V. Springel, S. D. M. White, J. Wang, C. S. Frenk, A. Jenkins, A. Ludlow, and J. F. Navarro, Phase-space structure in the local dark matter distribution and its signature in direct detection experiments, Mon. Not. R. Astron. Soc. **395**, 797 (2009).
[26] M. Kuhlen, N. Weiner, J. Diemand, P. Madau, B. Moore, D. Potter, J. Stadel, and M. Zemp, Dark matter direct detection with non-Maxwellian velocity structure, J. Cosmol. Astropart. Phys. 02 (2010) 030.
[27] Y. Y. Mao, L. E. Strigari, R. H. Wechsler, H. Y. Wu, and O. Hahn, Halo-to-halo similarity and scatter in the velocity distribution of dark matter, Astrophys. J. **764**, 35 (2013).
[28] K. Freese, P. Gondolo, and H. J. Newberg, Detectability of weakly interacting massive particles in the Sagittarius dwarf tidal stream, Phys. Rev. D **71**, 043516 (2005).
[29] C. W. Purcell, A. R. Zentner, and M. Y. Wang, Dark matter direct search rates in simulations of the Milky Way and Sagittarius stream, J. Cosmol. Astropart. Phys. 08 (2012) 027.
[30] F. S. Ling, Is the dark disc contribution to dark matter signals important?, Phys. Rev. D **82**, 023534 (2010).
[31] T. Bruch, J. Read, L. Baudis, and G. Lake, Detecting the Milky Way's dark disk, Astrophys. J. **696**, 920 (2009).
[32] J. I. Read, G. Lake, O. Agertz, and V. P. Debattista, Thin, thick and dark discs in LCDM, Mon. Not. R. Astron. Soc. **389**, 1041 (2008).

[33] J. I. Read, L. Mayer, A. M. Brooks, F. Governato, and G. Lake, A dark matter disc in three cosmological simulations of Milky Way mass galaxies, Mon. Not. R. Astron. Soc. **397**, 44 (2009).
[34] M. Lisanti and D. N. Spergel, Dark matter debris flows in the Milky Way, Phys. Dark Univ. **1**, 155 (2012).
[35] M. Kuhlen, M. Lisanti, and D. N. Spergel, Direct detection of dark matter debris flows, Phys. Rev. D **86**, 063505 (2012).
[36] C. Savage, K. Freese, and P. Gondolo, Annual modulation of dark matter in the presence of streams, Phys. Rev. D **74**, 043531 (2006).
[37] S. K. Lee and A. H. G. Peter, Probing the local velocity distribution of WIMP dark matter with directional detectors, J. Cosmol. Astropart. Phys. 04 (2012) 029.
[38] C. A. J. O'Hare and A. M. Green, Directional detection of dark matter streams, Phys. Rev. D **90**, 123511 (2014).
[39] C. McCabe, The astrophysical uncertainties of dark matter direct detection experiments, Phys. Rev. D **82**, 023530 (2010).
[40] M. T. Frandsen, F. Kahlhoefer, C. McCabe, S. Sarkar, and K. Schmidt-Hoberg, Resolving astrophysical uncertainties in dark matter direct detection, J. Cosmol. Astropart. Phys. 01 (2012) 024.
[41] A. Friedland and I. M. Shoemaker, Integrating in dark matter astrophysics at direct detection experiments, Phys. Lett. B **724**, 183 (2013).
[42] B. Feldstein and F. Kahlhoefer, A new halo-independent approach to dark matter direct detection analysis, J. Cosmol. Astropart. Phys. 08 (2014) 065.
[43] A. J. Anderson, P. J. Fox, Y. Kahn, and M. McCullough, Halo-independent direct detection analyses without mass assumptions, J. Cosmol. Astropart. Phys. 10 (2015) 012.
[44] J. D. Lewin and P. F. Smith, Review of mathematics, numerical factors, and corrections for dark matter experiments based on elastic nuclear recoil, Astropart. Phys. **6**, 87 (1996).
[45] A. K. Drukier, K. Freese, and D. N. Spergel, Detecting cold dark matter candidates, Phys. Rev. D **33**, 3495 (1986).
[46] D. Z. Freedman, Coherent neutrino nucleus scattering as a probe of the weak neutral current, Phys. Rev. D **9**, 1389 (1974).
[47] N. Mirabolfathi, H. R. Harris, R. Mahapatra, K. Sundqvist, A. Jastram, B. Serfass, D. Faiez, and B. Sadoulet, Toward single electron resolution phonon mediated ionization detectors, arXiv:1510.00999.
[48] L. E. Strigari, The neutrino floor at ultra-low threshold, Phys. Rev. D **93**, 103534 (2016).
[49] J. Billard, L. E. Strigari, and E. Figueroa-Feliciano, Solar neutrino physics with low-threshold dark matter detectors, Phys. Rev. D **91**, 095023 (2015).
[50] D. G. Cerdeo, M. Fairbairn, T. Jubb, P. A. N. Machado, A. C. Vincent, and C. Boehm, Physics from solar neutrinos in dark matter direct detection experiments, J. High Energy Phys. 05 (2016) 118.
[51] A. M. Serenelli, W. C. Haxton, and C. Peña-Garay, Solar models with accretion. I. Application to the solar abundance problem, Astrophys. J. **743**, 24 (2011).
[52] J. Bergstrom, M. C. Gonzalez-Garcia, M. Maltoni, C. Peña-Garay, A. M. Serenelli, and N. Song, Updated determination of the solar neutrino fluxes from solar neutrino data, J. High Energy Phys. 03 (2016) 132.
[53] J. F. Beacom, The diffuse supernova neutrino background, Annu. Rev. Nucl. Part. Sci. **60**, 439 (2010).
[54] M. Honda, T. Kajita, K. Kasahara, and S. Midorikawa, Improvement of low energy atmospheric neutrino flux calculation using the JAM nuclear interaction model, Phys. Rev. D **83**, 123001 (2011).
[55] W. C. Haxton, R. G. Hamish Robertson, and A. M. Serenelli, Solar neutrinos: Status and prospects, Annu. Rev. Astron. Astrophys. **51**, 21 (2013).
[56] V. Antonelli, L. Miramonti, C. Peña Garay, and A. Serenelli, Solar neutrinos, Adv. High Energy Phys. **2013**, 351926 (2013).
[57] G. Bellini *et al.* (BOREXINO Collaboration), Neutrinos from the primary proton–proton fusion process in the Sun, Nature (London) **512**, 383 (2014).
[58] N. Grevesse and A. J. Sauval, Standard solar composition, Space Sci. Rev. **85**, 161 (1998).
[59] E. G. Adelberger *et al.*, Solar fusion cross sections II: The pp chain and CNO cycles, Rev. Mod. Phys. **83**, 195 (2011).
[60] G. Battistoni, A. Ferrari, T. Montaruli, and P. R. Sala, The atmospheric neutrino flux below 100-MeV: The FLUKA results, Astropart. Phys. **23**, 526 (2005).
[61] G. Battistoni, A. Ferrari, T. Montaruli, and P. R. Sala, The FLUKA atmospheric neutrino flux calculation, Astropart. Phys. **19**, 269 (2003).
[62] G. Cowan, K. Cranmer, E. Gross, and O. Vitells, Asymptotic formulae for likelihood-based tests of new physics, Eur. Phys. J. C **71**, 1554 (2011); Eur. Phys. J. C **73**, 2501(E) (2013).
[63] J. Aalbers *et al.* (DARWIN Collaboration), DARWIN: Towards the ultimate dark matter detector, arXiv:1606.07001.
[64] P. J. T. Leonard and S. Tremaine, The local Galactic escape speed, Astrophys. J. **353**, 486 (1990).
[65] M. Steinmetz *et al.*, The Radial Velocity Experiment (RAVE): First data release, Astron. J. **132**, 1645 (2006).
[66] M. C. Smith *et al.*, The RAVE Survey: Constraining the local Galactic escape speed, Mon. Not. R. Astron. Soc. **379**, 755 (2007).
[67] T. Piffl *et al.*, The RAVE survey: The Galactic escape speed and the mass of the Milky Way, Astron. Astrophys. **562**, A91 (2014).
[68] N. Bozorgnia, G. B. Gelmini, and P. Gondolo, Daily modulation due to channeling in direct dark matter crystalline detectors, Phys. Rev. D **84**, 023516 (2011).
[69] R. Schoenrich, J. Binney, and W. Dehnen, Local kinematics and the local standard of rest, Mon. Not. R. Astron. Soc. **403**, 1829 (2010).
[70] F. J. Kerr and D. Lynden-Bell, Review of galactic constants, Mon. Not. R. Astron. Soc. **221**, 1023 (1986).
[71] J. Lavalle and S. Magni, Making sense of the local Galactic escape speed estimates in direct dark matter searches, Phys. Rev. D **91**, 023510 (2015).
[72] M. J. Reid *et al.*, Trigonometric parallaxes of high mass star forming regions: The structure and kinematics of the Milky Way, Astrophys. J. **783**, 130 (2014).

[73] O. Bienaym *et al.*, Weighing the local dark matter with RAVE red clump stars, Astron. Astrophys. **571**, A92 (2014).
[74] M. Lisanti, L. E. Strigari, J. G. Wacker, and R. H. Wechsler, The dark matter at the end of the Galaxy, Phys. Rev. D **83**, 023519 (2011).
[75] F. S. Ling, E. Nezri, E. Athanassoula, and R. Teyssier, Dark matter direct detection signals inferred from a cosmological N-body simulation with baryons, J. Cosmol. Astropart. Phys. 02 (2010) 012.
[76] N. Bozorgnia, F. Calore, M. Schaller, M. Lovell, G. Bertone, C. S. Frenk, R. A. Crain, J. F. Navarro, J. Schaye, and T. Theuns, Simulated Milky Way analogues: Implications for dark matter direct searches, J. Cosmol. Astropart. Phys. 05 (2016) 024.
[77] C. Kelso, C. Savage, M. Valluri, K. Freese, G. S. Stinson, and J. Bailin, The impact of baryons on the direct detection of dark matter, J. Cosmol. Astropart. Phys. 08 (2016) 071.
[78] J. D. Sloane, M. R. Buckley, A. M. Brooks, and F. Governato, Assessing astrophysical uncertainties in direct detection with galaxy simulations, arXiv:1601.05402.
[79] B. J. Kavanagh, Parametrizing the local dark matter speed distribution: A detailed analysis, Phys. Rev. D **89**, 085026 (2014).
[80] S. K. Lee, Harmonics in the dark-matter sky: Directional detection in the Fourier-Bessel basis, J. Cosmol. Astropart. Phys. 03 (2014) 047.
[81] J. Stadel, D. Potter, B. Moore, J. Diemand, P. Madau, M. Zemp, M. Kuhlen, and V. Quilis, Quantifying the heart of darkness with GHALO: A multi-billion particle simulation of our galactic halo, Mon. Not. R. Astron. Soc. **398**, L21 (2009).
[82] M. T. Busha, A. E. Evrard, F. C. Adams, and R. H. Wechsler, The ultimate halo mass in a Lambda-CDM universe, Mon. Not. R. Astron. Soc. **363**, L11 (2005).
[83] Y. Y. Mao, L. E. Strigari, and R. H. Wechsler, Connecting direct dark matter detection experiments to cosmologically motivated halo models, Phys. Rev. D **89**, 063513 (2014).
[84] G. Angloher *et al.* (CRESST Collaboration), Results on light dark matter particles with a low-threshold CRESST-II detector, Eur. Phys. J. C **76**, 25 (2016).
[85] R. Agnese *et al.* (SuperCDMS Collaboration), New Results from the Search for Low-Mass Weakly Interacting Massive Particles with the CDMS Low Ionization Threshold Experiment, Phys. Rev. Lett. **116**, 071301 (2016).
[86] F. Feroz and M. P. Hobson, Multimodal nested sampling: An efficient and robust alternative to MCMC methods for astronomical data analysis, Mon. Not. R. Astron. Soc. **384**, 449 (2008).
[87] F. Feroz, M. P. Hobson, and M. Bridges, MultiNest: An efficient and robust Bayesian inference tool for cosmology and particle physics, Mon. Not. R. Astron. Soc. **398**, 1601 (2009).
[88] F. Feroz, M. P. Hobson, E. Cameron, and A. N. Pettitt, Importance nested sampling and the MultiNest algorithm, arXiv:1306.2144.